

## The Growth of Black Holes and Their Host Spheroids in (Sub)mm-loud QSOs at High Redshift

C.N. Hao<sup>1,2,3\*</sup>, X.Y. Xia<sup>1</sup>, S. Mao<sup>4</sup>, Z.G. Deng<sup>5</sup> and Hong Wu<sup>2</sup>

<sup>1</sup> Center of Astrophysics, Tianjin Normal University, 300384 Tianjin, China

<sup>2</sup> National Astronomical Observatories, Chinese Academy of Sciences, A20 Datun Road, 100012 Beijing, China

<sup>3</sup> Current address: Institute of Astronomy, University of Cambridge, Madingley Road, Cambridge CB3 0HA, UK

<sup>4</sup> Jodrell Bank Observatory, University of Manchester, Macclesfield, Cheshire SK11 9DL, UK

<sup>5</sup> College of Physical Science, Graduate School of the Chinese Academy of Sciences, Beijing 100049, China

**Abstract** We study the growth of black holes and stellar population in spheroids at high redshift using several (sub)mm-loud QSO samples. Applying the same criteria established in an earlier work, we find that, similar to IR QSOs at low redshift, the far-infrared emission of these (sub)mm-loud QSOs mainly originates from dust heated by starbursts. By combining low- $z$  IR QSOs and high- $z$  (sub)mm-loud QSOs, we find a trend that the star formation rate ( $\dot{M}_*$ ) increases with the accretion rate ( $\dot{M}_{acc}$ ). We compare the values of  $\dot{M}_*/\dot{M}_{acc}$  for submm emitting galaxies (SMGs), far-infrared ultraluminous/hyperluminous QSOs and typical QSOs, and construct a likely evolution scenario for these objects. The (sub)mm-loud QSO transition phase has both high  $\dot{M}_{acc}$  and  $\dot{M}_*$  and hence is important for establishing the correlation between the masses of black holes and spheroids.

**Key words:** galaxies: active — galaxies: evolution — galaxies: high redshift — galaxies: interactions — quasars: general — galaxies: starburst

### 1 INTRODUCTION

In the last few years, it has become increasingly clear that the growth of supermassive black holes and their host spheroids must be closely related as the black hole mass has correlations with the galactic velocity dispersion (e.g., Ferrarese & Merritt 2000; Tremaine et al. 2002) and the luminosity/mass of the hot stellar component of the host galaxy (e.g., Magorrian et al. 1998; Laor 1998; Kormendy & Gebhardt 2001).

---

\* E-mail: hcn@ast.cam.ac.uk

However, it remains unclear how the correlations arise. Although much effort has been made both theoretically (e.g. Silk & Rees 1998; Haehnelt & Kauffmann 2000; Adams et al. 2001; Burkert & Silk 2001; Balberg & Shapiro 2002; Springel et al. 2005; Di Matteo et al. 2005) and observationally (e.g. Shields et al. 2003; Treu et al. 2004; Heckman et al. 2004; Walter et al. 2004; Borys et al. 2005; Shields et al. 2006), the definitive interpretation still remains to be established.

In an earlier work, Hao et al. (2005) studied the QSOs/Seyfert 1s selected from local ultraluminous infrared galaxies (IR QSOs) and found a correlation between the star formation rate ( $\dot{M}_*$ ) and the accretion rate to central AGNs ( $\dot{M}_{\text{acc}}$ ) for IR QSOs; the ratio of  $\dot{M}_*$  to  $\dot{M}_{\text{acc}}$  is about several hundred (Hao et al. 2005, hereafter paper I). These IR QSOs not only have massive starbursts occurring in their host galaxies their optical spectroscopic and X-ray properties also exhibit characteristics of young forming QSOs (Zheng et al. 2002). Thus IR QSOs may be an important evolution phase from massive starbursts to luminous QSOs and later to elliptical galaxies. During this transition phase, both the spheroid components and central black holes grow rapidly. Therefore it is important to extend our previous studies for the local universe to high redshift in order to better understand how the correlation between the masses of spheroids and their central black holes arises and evolves as a function of cosmic time.

Massive submillimeter emitting galaxies (SMGs), uncovered by deep SCUBA surveys on blank fields, resemble scaled-up versions of the local ultraluminous infrared galaxies at high redshift (e.g. Tacconi et al. 2006) – their star formation rates and molecular gas reservoirs are one order of magnitude higher (on average) than their counterparts at low redshift (e.g. Kim et al. 1998; Downes & Solomon 1998; Chapman et al. 2004; Alexander et al. 2005b). In addition, recent investigations on SMGs by ultra-deep X-ray observations (the 2 Ms Chandra Deep Field North) reveal only modest  $\dot{M}_{\text{acc}} \lesssim 1M_{\odot} \text{yr}^{-1}$  for their central AGNs (Alexander et al. 2005a,b). These observations indicate that there are few luminous QSOs in the current SMG samples and hence they are not ideal samples from which we can identify high- $z$  analogues of local IR QSOs. On the other hand, targeted observations of high- $z$  QSOs at submillimeter (submm) wavelength reveal a category of submm-loud QSOs (e.g., McMahan et al. 1999; Isaak et al. 2002). The average redshift and submm flux density of these submm detected QSOs by Stevens et al. (2005) are consistent with SMGs, but their median X-ray flux is 30 times higher than those of SMGs selected from blank surveys, indicating much higher  $\dot{M}_{\text{acc}}$  than those of SMGs (see also Alexander et al. 2005b). Similarly, the average redshift and submm flux density of submm detected bright QSOs by Priddey et al. (2003a) are also comparable to those of X-ray selected QSOs by Stevens et al. (2005). Note also that most submm-loud QSOs by Isaak et al. (2002) have also been detected at 1.2 mm by Omont et al. (2001).

Given that several groups have investigated the properties of high- $z$  bright QSO samples using targeted (sub)mm observations (e.g. Carilli et al. 2001; Omont et al. 2001, 2003; Priddey et al. 2003a,b; Stevens et al. 2005), it is natural to search from these samples the high- $z$  analogues of the local IR QSOs, and study their physical properties. We are particularly interested in how the star formation and accretion processes are related to each other in the extreme environments and which of these dominates the heating of dust that gives rise to the rest-frame (thermal) submm emissions (e.g., Carilli et al. 2001; Isaak et al. 2002). To achieve this, we extend the technique developed in Paper I to the high- $z$  (sub)mm observed QSO samples. This paper is structured as follows. In Sect. 2, we describe how the samples are compiled. In Sect. 3, we discuss how

physical parameters are estimated. The main results are presented and discussed in Sect. 4. Finally, in Sect. 5, we briefly summarize our results. Throughout this paper we adopt a cosmology with a matter density parameter  $\Omega_m = 0.3$ , a cosmological constant  $\Omega_\Lambda = 0.7$  and a Hubble constant of  $H_0 = 70 \text{ km s}^{-1} \text{ Mpc}^{-1}$ .

## 2 SAMPLES

As discussed above, high- $z$  QSO samples with submm or mm wavelength observations are needed for our purpose. First we collect several high- $z$  optically selected QSO samples with mm (1.2 mm) observations, taken from Carilli et al. (2001) and Omont et al. (2001, 2003). The 1.2 mm observations were made using the Max-Planck Millimeter Bolometer (MAMBO; Kreysa et al. 1998) on the IRAM 30m telescope on Pico Veleta in Spain. The details are listed below. Note that the  $B$ -band absolute magnitudes ( $M_B$ ) in the following descriptions are taken directly from the cited papers, appropriate for a cosmology with  $H_0 = 50 \text{ km s}^{-1} \text{ Mpc}^{-1}$ ,  $\Omega_m = 1$  and  $\Omega_\Lambda = 0$ .

- (1) A QSO sample taken from Carilli et al. (2001) consists of 41 sources, which were found in the Sloan Digital Sky Survey (SDSS). They span a range of  $M_B = -26.1$  to  $-28.8$  and a redshift range from  $z = 3.6$  to  $5.0$ . 16 out of 41 objects have 1.2 mm flux densities 3 times greater than the rms noise ( $3\sigma$ ).
- (2) A QSO sample taken from Omont et al. (2001) consists of 65 objects, which were selected from Palomar Sky Survey (PSS). They have  $M_B < -27.0$  and  $3.9 < z < 4.5$ . 21 out of these 65 objects were detected with flux densities greater than  $3\sigma$  at 1.2 mm.
- (3) An optically luminous ( $M_B < -27.0$ ) but radio quiet QSO sample taken from Omont et al. (2003) consists of 35 objects at redshift  $1.8 < z < 2.8$ . 9 were detected at 1.2 mm with flux densities at levels  $\geq 3\sigma$ .

As the Submillimeter Common User Bolometer Array (SCUBA) detector on the JCMT has similar capabilities with MAMBO, we also collect high- $z$  optically selected QSO samples observed at submm ( $850\mu\text{m}$ ), taken from McMahon et al. (1999), Isaak et al. (2002) and Priddey et al. (2003a,b):

- (1) An optically luminous ( $M_B < -27$ ) and radio quiet QSO sample from McMahon et al. (1999) with redshift  $z \gtrsim 4$ . 7 out of the 10 QSOs were detected at levels  $\geq 3\sigma$  at  $850\mu\text{m}$ .
- (2) An optically luminous ( $M_B < -27.5$ ) and radio quiet QSO sample from Isaak et al. (2002) consists of 38 objects with redshift  $z \geq 4$ . 8 were detected at  $850\mu\text{m}$  with flux densities at levels  $\geq 3\sigma$ .
- (3) An optically luminous ( $M_B < -27.5$ ) and radio quiet QSO sample taken from Priddey et al. (2003a) consists of 57 objects with redshift  $1.5 < z < 3.0$ . 9 were detected at  $850\mu\text{m}$  with flux densities at levels  $\geq 3\sigma$ .
- (4) An optically selected QSO sample with redshift  $> 4.9$  from Priddey et al. (2003b) consists of 14 objects, among which 4 were detected at  $850\mu\text{m}$  at  $\geq 4\sigma$  levels (see Priddey et al. 2003b for detail).

In the following, we denote high- $z$  sources as detected (non-detected) at 1.2 mm or at  $850\mu\text{m}$  if their flux densities are above (below) three times the rms noise level.

Besides these mm (1.2 mm) and submm ( $850\mu\text{m}$ ) observed high- $z$  QSOs samples, we also collect high- $z$  QSOs with ultraluminous or hyperluminous FIR luminosities ( $> 10^{12}$  or  $10^{13} L_\odot$ ) detected by other means, to verify the assumption in our method as many of them have unambiguous starbursts which

dominate their infrared emissions (see §4.1; Stevens et al. 2005; Carilli et al. 2005). Specifically, we include (1) 19 X-ray absorbed, Compton-thin QSOs with submm ( $450\mu\text{m}$  and  $850\mu\text{m}$ ) photometry (Stevens et al. 2005), among which 8 were detected at  $850\mu\text{m}$ , and for comparison, 19 X-ray unabsorbed QSOs observed but non-detected at submm ( $850\mu\text{m}$ , Page et al. 2004). The submm photometry observations at  $450\mu\text{m}$  and  $850\mu\text{m}$  for these QSOs were performed using SCUBA. The redshift range of this sample is  $1 < z < 3$ . Note that two of the X-ray absorbed, Compton thin QSOs treated as detections were observed with  $2 < S/N < 3$  as indicated by Stevens et al. (2005). (2) two high- $z$  QSOs (B1202–0725 and J1148+5251) with HCN and CO observations (Carilli et al. 2002; Walter et al. 2003; Isaak et al. 2004; Carilli et al. 2005) and one (B1335–0417) with only CO detections (Carilli et al. 2002). The  $B$ -band absolute luminosity and 1.25 mm flux densities for B1202–0725 and B1335–0417 are adopted from Omont et al. (1996); for J1148+5251, they are taken from Robson et al. (2004) and Bertoldi et al. (2003) respectively.

The comparison samples at low redshift are taken from paper I. Briefly, these include an IR QSO sample, an optically selected Palomar-Green QSO (PG QSO) sample, and a narrow-line Seyfert 1 galaxy (NLS1) sample. IR luminosities and bolometric luminosities are available for all these objects (see paper I for details).

As described above, most target QSOs were compiled from heterogeneous flux-limited samples, so they likely suffer from some selection biases. For example, QSOs at the bright end of the luminosity function (with high  $\dot{M}_{\text{acc}}$ ) are favored in our samples. Nevertheless, the selection of high  $\dot{M}_{\text{acc}}$  objects will not have significant impacts on our results as our main purpose is to compare the relative growth of black holes and spheroids (i.e., the ratio of  $\dot{M}_*$  and  $\dot{M}_{\text{acc}}$ ); we return to this point in Sect. 4.2.

### 3 ESTIMATION OF PHYSICAL PARAMETERS

For the local sample, the values of various physical parameters except the star formation rate (see §3.2) were taken directly from paper I; we refer the readers to that paper for detail. Below we discuss how we derive the physical parameters for the high- $z$  objects and the values are listed in Tables 1 and 3 for mm and submm detected QSOs respectively.

#### 3.1 Accretion Rates

The accretion rates are derived from the bolometric luminosities following the formula given in paper I:

$$\dot{M}_{\text{acc}} = 6.74 M_{\odot} \text{yr}^{-1} \frac{L_{\text{bol}}}{10^{13} L_{\odot}}. \quad (1)$$

For the objects not selected from X-ray observations, the bolometric luminosities were estimated from the absolute  $B$ -band magnitude converted to our adopted cosmology. A bolometric correction factor of 9.74 was adopted according to Vestergaard (2004). For the X-ray selected QSOs, the bolometric luminosities are calculated from the X-ray luminosities,  $L_X$  (0.5 – 2 KeV), adopting a value of 33.3 as the bolometric correction factor (Stevens et al. 2005). The bolometric luminosities derived using two different methods are on average in agreement with each other. This can be seen from the application of these two methods to the X-ray absorbed QSOs that also have  $B$ -band magnitudes.

### 3.2 Star Formation Rates

The star formation rates are estimated from the monochromatic luminosities at  $60\mu\text{m}$  ( $\mathbb{L}60 = \nu L_\nu(60\mu\text{m})$ ),

$$\dot{M}_* \approx 3.26 M_\odot \text{yr}^{-1} \frac{L_{60\mu\text{m}}}{10^{10} L_\odot}. \quad (2)$$

This equation is obtained by the application of the conversion factors among the luminosities with different infrared wavelength coverage to the Kennicutt star formation rate law (Kennicutt 1998; see paper I for details). The star formation rate derived using equation (2) is  $\sim 50\%$  of that using the formula given in paper I. This is because we find that the FIR luminosity between  $40$  and  $120\mu\text{m}$  in our case (for local IR QSOs) is roughly equal to, rather than a factor of two of,  $\mathbb{L}60$ , as assumed in Paper I (see also Martin et al. 2005). This downward revision is also consistent with the prescription given by Rowan-Robinson (2000). Therefore, we recalculated  $\dot{M}_*$  for IR QSOs using equation (2). This does not, however, affect our main conclusions in paper I (as the scatter around the mean relation is large).

For  $1.2$  mm detected high- $z$  QSOs, we estimated the rest-frame monochromatic luminosity at  $60\mu\text{m}$  from the observed flux density at  $1.2$  mm by assuming that the rest-frame FIR spectral energy distribution (SED) can be described by a greybody spectrum with a dust temperature of  $41$  K and a dust emissivity index ( $\beta$ ) of  $1.95$ . These parameters were derived by Priddey & McMahon (2001) by fitting the photometric measurements at submm and mm wavebands for several high- $z$  ( $z > 4$ ) quasars. Specifically, for QSOs with  $1.2$  mm observations, we apply the  $k$ -correction and obtain the rest-frame flux density at  $1.2$  mm/ $(1+z)$ ; this step fixes the overall normalization of the greybody SED template, which can then be used to derive the rest-frame flux density at  $60\mu\text{m}$ . The star formation rate is then obtained using equation (2). For the X-ray selected and other  $850\mu\text{m}$  detected QSOs, the same method is applied at  $850\mu\text{m}$  instead of  $1.2$  mm.

In previous studies, an assumption of a rest-frame FIR SED with a dust temperature of  $\sim 50$  K and a dust emissivity index of  $\beta \sim 1.5$  is often used (e.g. Omont et al. 2001; Carilli et al. 2001). Recent studies of the SEDs of more than ten high- $z$  QSOs give a best-fit of temperature of  $52 \pm 3$  K and a dust emissivity index of  $\beta = 1.5 \pm 0.1$ , with individual dust temperatures ranging from  $40$  to  $60$  K (Beelen et al. 2006). If we adopt these dust parameter values, rather than the Priddey & McMahon (2001) SED fitting results, our estimates of  $\mathbb{L}60$  are changed by only  $\sim 20 - 30\%$ . However, when the individual dust temperature differences ( $40$ - $60$ K) are concerned, the estimates will be changed by more than  $0.5$  dex for  $\beta = 1.5 \pm 0.1$ .

It is worth noting that the prescription we used here to obtain the star formation rate differs from that adopted by Carilli et al. (2001) and Omont et al. (2001, 2003), which gives a star formation rate that is several times lower than that from eq. (2). The differences arise from different methods in deriving the IR or FIR luminosity, and different assumptions about the initial mass function, stellar evolutionary theory and the wavebands in which the absorbed starburst's total luminosity is re-emitted. As discussed by Kennicutt (1998), the star formation rates derived with different methods depend on a number of assumptions and are not precise; each method offers a useful means of estimating the star formation activity. For consistency, we use eq. (2) to estimate the  $\dot{M}_*$  for objects in the local universe and at high redshift.

## 4 RESULTS AND DISCUSSIONS

### 4.1 (Sub)mm-Quiet and (Sub)mm-Loud QSOs

Fig. 1a shows the rest-frame monochromatic luminosity at  $60\mu\text{m}$ ,  $L_{60}$ , versus the bolometric luminosity associated with the central AGNs for all low- $z$  sources and the 1.2 mm observed high- $z$  QSOs. The regression line in Fig. 1a is the best fit line for low- $z$  typical type 1 AGNs (PG QSOs and NLS1s). The close correlation between  $L_{60}$  and  $L_{\text{bol}}$  for low- $z$  typical type 1 AGNs suggests that their FIR emissions are mainly powered by the central AGNs (see paper I and Haas et al. 2003). It is clear from Fig. 1a that all the high- $z$  QSOs detected at 1.2 mm are located above the regression line just as the low- $z$  IR QSOs.

The majority ( $\sim 70\%$ ) of optically selected QSOs are, however, not detected at 1.2 mm above the  $3\sigma$  level (e.g. Carilli et al. 2004; Momjian et al. 2005). We use the stacking method (see Stevens et al. 2005) to obtain the mean value of the rest-frame  $L_{60}$  for the 95 QSOs not detected at 1.2 mm. For each sample (see Sect. 2), we divide the redshift into bins with width of  $\approx 0.5$ . The bolometric luminosity is simply the average of the objects in each bin. The 1.2 mm flux density is obtained as the mean of the sources in each bin weighted by their uncertainties. The rest-frame  $L_{60}$  is calculated in the way as described in Sect. 3.2, with the obtained mean flux densities and the mean bin redshift. The error bars of the binned data are calculated using error propagation by weighting the uncertainties of the observed flux densities at 1.2 mm. The results from stacking are listed in Table 2 and plotted in Fig. 1a. It is striking that these data points are all around the regression line inferred from the low- $z$  typical type 1 AGNs.

A similar analysis was performed for high- $z$  QSOs observed at  $850\mu\text{m}$  (instead of 1.2mm). These include QSOs selected optically and from X-ray (see Sect. 2). Fig. 1b shows  $L_{60}$  vs.  $L_{\text{bol}}$  for all low- $z$  type 1 AGNs, IR QSOs, high- $z$  submm detected QSOs and submm non-detected QSOs. Fig. 1b clearly shows that all  $850\mu\text{m}$  non-detected QSOs except the X-ray absorbed ones are around the regression line derived from low- $z$  type 1 AGNs. In contrast, all the  $850\mu\text{m}$  detected QSOs are above this regression line.

The similar behaviours of high- $z$  QSOs observed at  $850\mu\text{m}$  by SCUBA and those observed at 1.2 mm by MAMBO in the relation of FIR luminosities to bolometric luminosities show that the difference between (sub)mm detected and non-detected QSOs may be real, rather than from the effects of instrument sensitivities. In fact, the samples used here were observed with different sensitivities, even for measurements taken by the same instrument. For 1.2 mm observations by MAMBO, the typical rms sensitivities vary from 0.5 mJy to 1.4mJy; while for  $850\mu\text{m}$  observations by SCUBA, the sensitivities of the surveys change from 1.5 mJy to 3.3 mJy. In a word, the sensitivities vary by a factor of 2-3 for different observations (e.g. Omont et al. 2001, 2003; Carilli et al. 2001; MaMchon et al. 1999; Issak et al. 2002). Observations with different sensitivities lead to significantly different weighted mean flux densities for non-detected QSOs shown in Tables 2 and 4. Nevertheless, the positions of the (sub)mm non-detected QSOs are not strongly influenced by the sensitivities as they are all located around the regression line inferred for low- $z$  typical QSOs. This suggests that the high- $z$  (sub)mm non-detected QSOs may be the analogues of typical QSOs seen locally and the FIR emission from these high- $z$  objects are powered by AGNs, just as the low- $z$  typical QSOs. Of course, the high- $z$  QSOs have higher accretion rates than their local counterparts.

On the other hand, for high- $z$  QSOs detected at 1.2 mm and  $850\mu\text{m}$ , their rest-frame  $L_{60}$  are all above the regression line for typical QSOs, implying that

these objects are the analogues of low- $z$  IR QSOs. For both the local and high- $z$  samples, the excess FIR emission relative to the regression lines is probably provided by an additional energy source, namely massive starbursts in these objects.

Our conclusions are supported by the CO and/or HCN observations for three additional high- $z$  QSOs (B1335–0417, B1202–0725 and J1148+5251, shown as crosses in Fig. 1a and Fig. 1b), which revealed massive molecular gas reservoirs in these three QSOs ( $10^{10}$  to  $10^{11} M_{\odot}$ , e.g., Carilli et al. 2002, 2004; Walter et al. 2003, 2004). Therefore, massive starbursts are occurring at the host spheroids of these objects and provide the dominant energy source which heats the dust. In Fig. 1a and Fig. 1b, these three QSOs are clearly located above the regression line for typical QSOs and they mix well with all the (sub)mm detected QSOs. In addition, two 1.2 mm detected QSOs (J140955.5+562827, Omont 2003, and PSS J2322+1944, Omont 2001, shown as crossed squares in Fig. 1a and Fig. 1b) have also been detected by CO observations. Note that only 1 (PSS J2322+1944) out of these 5 QSOs are magnified by gravitational lensing. In any case, lensing magnification should not be statistically important for most of our objects according to Vestergaard (2004).

In fact, using deep radio observations, it has already been suggested that the physics of submm-loud QSOs and submm-quiet QSOs may be different (Petric & Carilli 2004). Furthermore, the extended dust emission regions (larger than 1 kpc) of (sub)mm-loud QSOs rule out the central AGN heating model (e.g., Momjian et al. 2005 and references therein). Stevens et al. (2005) also argued that the submm emission of submm detected, X-ray absorbed QSOs is attributed to dust heated by hot young stars. The approach we adopt here is different but we reach the same conclusion – the high- $z$  (sub)mm-loud QSOs are low- $z$  analogues of IR QSOs and their ultraluminous/hyperluminous FIR emissions are mainly from dust heated by massive starbursts. As we show below, they are at a transition phase with rapid growth of black holes and their host spheroids.

#### 4.2 Coeval Growth of Black Holes and Host Spheroids

Given that the ultraluminous/hyperluminous FIR emissions are mainly from dust heated by massive starbursts for both low- $z$  IR QSOs and high- $z$  (sub)mm-loud QSOs, we can estimate the star formation rates for these high- $z$  (sub)mm-loud QSOs using the same method as that for low- $z$  IR QSOs. The star formation rates are estimated from  $L_{60}$ , after subtracting the contribution from the central AGNs, namely assuming the AGN contribution to  $L_{60}$  for (sub)mm-loud QSOs follows the same regression line as typical QSOs shown as the solid line in Fig. 1.

Fig. 2a and b shows the star formation rate versus the accretion rate for IR QSOs and high- $z$  (sub)mm-loud QSOs. It is obvious from Fig. 2 that for QSOs with larger accretion rates and hence higher bolometric luminosities, their star formation rates are also higher. This trend directly indicates that the massive galaxies build their spheroid stellar masses and central black holes quicker than less massive ones, and hence the most massive galaxies host the most luminous QSOs in their centers. Although this trend has been noticed in paper I, the combination of high- $z$  (sub)mm-loud QSOs with the local IR QSOs provides a much larger dynamical range for studying the relation between  $\dot{M}_{\star}$  and  $\dot{M}_{\text{acc}}$  than either sample alone. This is appropriate because the underlying physics of QSOs at low and high redshift may be similar (Fan et al. 2004; Vestergaard 2004 and references therein; see also below). Thus we can extend the dynamic range in the bolometric luminosity by combining low- and high-redshift samples together. In contrast, this trend was not found based on high- $z$  (sub)mm observed QSOs alone (e.g. Isaak et al. 2002; Omont et al. 2003) because of limited dynamical range

and large scatters involved. In addition, the inclusion of both (sub)mm-loud and (sub)mm-quiet QSOs in previous analyses also obscures the trend as these two types of objects may be at physically different evolutionary stages (see below).

As can be seen from Fig. 2a and b, for a fixed  $\dot{M}_{\text{acc}}$ , there is roughly an order of magnitude scatter in  $\dot{M}_*$ . The large scatters may be partly because of the calibration errors in equation (2), and the differences in the FIR SED in QSOs. Nevertheless, it is quite likely that  $\dot{M}_*/\dot{M}_{\text{acc}}$  does vary from object to object. Therefore it is worth investigating how the  $\dot{M}_*/\dot{M}_{\text{acc}}$  changes with redshifts and bolometric luminosities of QSOs.

Fig. 3a and b shows  $\dot{M}_*/\dot{M}_{\text{acc}}$  versus redshift for low- $z$  IR QSOs and high- $z$  (sub)mm-loud QSOs. The sizes of the data points are scaled by their accretion rates, i.e., by their bolometric luminosities. It is obvious from Fig. 3a and b that there is an absence of QSOs with large  $\dot{M}_*/\dot{M}_{\text{acc}}$  at higher redshift. This may be caused by the Malmquist bias – for a flux-limited sample, as the redshift (distance) increases, more luminous objects are preferentially selected. In our case, the objects with lower accretion rates at high- $z$  could have been missed, although the samples we used here are not strictly flux-limited samples (most of our QSOs are optically luminous QSOs with  $M_B < -27.0$ ). To illustrate the influence of Malmquist bias quantitatively, we plot three dotted curves in Fig. 3a and b corresponding to a bolometric luminosity of  $10^{11}L_\odot$ ,  $10^{12}L_\odot$  and  $10^{13}L_\odot$  at redshift 2 respectively, which cover the whole range of the bolometric luminosity of low- $z$  IR QSOs. For each curve, we assume the relation between the star formation rate and the accretion rate by simply fitting a regression line to the data points in Fig. 2a using survival analysis (Isobe et al. 1986). In an optically selected flux-limited sample, the objects above these dotted lines will be missed during the observations with flux limits assumed above. From the shapes of these dotted lines, we can see that the higher ratios at lower redshift can be reproduced by the Malmquist bias, so the lack of high  $\dot{M}_*/\dot{M}_{\text{acc}}$  QSOs at high  $z$  may not be real.

There is a well-studied high- $z$  ( $z = 5.5$ ) optically faint ( $M_B \sim -24.2$ ) QSO – RDJ030117+002025 (e.g., Stern et al. 2000; Bertoldi & Cox 2002; Staghun et al. 2005) to test the above argument. The pentagram in all three figures represents this object. From the location of RDJ030117+002025 in Figs. 1-3, we can see that its behavior is similar to the low- $z$  IR QSOs. This suggests that at least some distant optically faint QSOs have similar properties to the low- $z$  IR QSOs, which also verifies the combination of low- $z$  IR QSOs and high- $z$  (sub)mm-loud QSOs in Fig. 2. However, more (sub)mm observations of high- $z$  optically faint QSOs are needed to firmly establish this.

On the other hand, it can be seen from Fig. 3a and b that the  $\dot{M}_*/\dot{M}_{\text{acc}}$  of the low- $z$  IR QSOs and high- $z$  (sub)mm-loud QSOs both have broad ranges and there is a clear trend that as the bolometric luminosity (indicated by the size of data points) increases, the  $\dot{M}_*/\dot{M}_{\text{acc}}$  decreases. Thus the behavior of the relative growth of host spheroids and their central black holes is correlated with the power of QSOs – the optically more luminous QSOs correspond to a phase with higher accretion rates and relatively low star formation rates, which results in the absence of optically luminous QSOs (shown as symbols with larger sizes in Fig. 3a and b) with large  $\dot{M}_*/\dot{M}_{\text{acc}}$ . This trend is consistent with the simulation prediction of Cattaneo et al. (2005, their Fig 11).

In Fig. 3a and b we also indicate the positions of SMGs (shown as pentagon) using their data in the Chandra Deep Field North with deep Keck spectroscopic data in Alexander et al. (2005b). The characteristic position of SMGs is obtained using the mean redshift and the mean  $\dot{M}_*/\dot{M}_{\text{acc}}$  in the Alexander et al. (2005b)



sample. It is clear from Fig. 3a and b that the SMGs are located above the FIR ultraluminous/hyperluminous QSOs.

The locations of SMGs and FIR ultraluminous/hyperluminous QSOs in Fig. 3 suggest a possible evolutionary picture in terms of  $\dot{M}_*/\dot{M}_{acc}$ , from top to bottom. SMGs represent prodigious starbursts triggered by interactions and major mergers as revealed by Hubble Space Telescope images in the rest-frame ultra-violet wavebands (Conselice et al. 2003; Smail et al. 2004). Although  $> 38_{-10}^{+12}\%$  SMGs host AGNs, the dominant rest-frame FIR energy output for most of them is still from starbursts (Alexander et al. 2005b) and this population is expected to be at a pre-QSO phase, during which the central black holes grow more slowly compared with their spheroids. As the gas falls toward the centers of galaxies, the accretion rate increases while the massive starbursts continue, experiencing a phase of simultaneous growth of central black holes and their spheroids. This coeval phase may be quite short ( $10^7$  to  $10^8$  years) if the (sub)mm-detected QSO fraction (20-30%) can be interpreted as the relative duty cycle (e.g. Carilli et al. 2004). The very high star formation rates and accretion rates in this phase lead to a rapid increase of the masses of the central black holes and spheroids. As the black hole mass increases, the central AGN becomes more energetic, and the AGN feedback process may heat up and blow away the surrounding gas and dust, leading to a decrease in the star formation rate and  $\dot{M}_*/\dot{M}_{acc}$ . Eventually, it enters the typical QSO phase with high accretion rate but low star formation rate. The QSOs at this stage will be located at the bottom of Fig. 3.

The picture described above corresponds well with the evolutionary sequence for low- $z$  gas-rich major mergers, from ultraluminous IR galaxies to IR QSOs (or FIR luminous Seyfert 1s; Sanders et al. 1988a,b), and finally to  $L^*$  elliptical galaxies. The difference is that high- $z$  SMGs have more gas and may evolve into giant elliptical galaxies. While not every single object may fit in this picture, e.g., the high- $z$  QSOs with large black hole mass and relatively low host dynamical mass may have a different evolutionary path, many ultraluminous IR galaxies (at low redshift) and SMGs (at high redshift) will evolve into  $L^*$  and giant ellipticals respectively along this path.

## 5 SUMMARY

In this paper we have examined the properties of high- $z$  QSOs samples observed at 1.2 mm, 850  $\mu$ m or with CO and/or HCN observations. The redshift of these objects spans from redshift 1 to 6.42. Applying the same criteria established for local type 1 AGNs (Hao et al. 2005), we found that statistically, the (sub)mm detected and non-detected high- $z$  QSOs are analogues of local IR QSOs and typical type 1 AGNs, respectively. We postulated that the underlying physics of (sub)mm detected and non-detected high- $z$  QSOs may be different, and they correspond to different phases in the interplay between AGNs and spheroids formation.

For (sub)mm-loud QSOs, the FIR ultraluminous/hyperluminous emissions are from dust heated predominantly by starbursts. By combining low- $z$  IR QSOs and high- $z$  (sub)mm-loud QSOs, we found a clear trend that the higher the accretion rate, the larger the star formation rate. It directly indicates that the most massive galaxies host the most luminous QSOs at their centers. We also found that the relative growth of black holes and their host spheroids depends on the intensity of QSO activities, in qualitative agreement with theoretical expectations. We also compared the properties of SMGs, ultraluminous or hyperluminous FIR QSOs and typical QSOs, and constructed a possible evolution scenario among

these objects. Clearly substantial growth of black holes and their host spheroids can occur in these objects. Future studies of these objects are therefore important for understanding how formation of spheroids and AGNs are inter-connected and how the  $M_{\text{BH}}-M_{\star}$  relation arises.

**Acknowledgements** We thank P. Cox, X. Fan and Y. Gao for advice and helpful discussions. Thanks are also due to R. Kennicutt for helpful discussions on the star formation rate estimators. This project is supported by the NSF of China 10333060 and 10778622. SM acknowledges partial travel support from the Chinese Academy of Sciences and a visiting professorship from Tianjin Normal University.

## References

- Adams F. C., Graff D. S., Richstone D. O. 2001, *ApJ*, 551, L31
- Alexander D. M., Smail I., Bauer F. E., Chapman S. C., Blain A. W., Brandt W. N., Ivison R. J. 2005, *Nature*, 434, 738 (2005a)
- Alexander D. M., Bauer F. E., Chapman S. C., Smail I., Blain A. W., Brandt W. N., Ivison R. J. 2005, *ApJ*, 632, 736
- Balberg S., Shapiro S. L. 2002, *Phys. Rev. Lett.*, 88, 101301
- Bertoldi F., Carilli C. L., Cox P., Fan X., Strauss M. A., Beelen A., Omont A., Zylka, R. 2003, *A&A*, 406, L55
- Bertoldi F., Cox P. 2002, *A&A*, 384, L11
- Borys C., Smail I., Chapman S. C., Blain A. W., Alexander D. M., Ivison R. J. 2005, *ApJ*, 635, 853
- Burkert A., Silk J. 2001, *ApJ*, 554, L151
- Carilli C. L. et al. 2001, *ApJ*, 555, 625
- Carilli C. L. et al. 2002, *AJ*, 123, 1838
- Carilli C. L., Bertoldi F., Walter F., Menten K. M., Beelen A., Cox P., Omont A. 2004, in *Proc. Multiwavelength AGN Surveys*, eds. R. Maiolino, R. Mujica, in press (astro-ph/0402573)
- Carilli C. L. et al. 2005, *ApJ*, 618, 586
- Cattaneo A., Blaizot J., Devriendt J., Guiderdoni B. 2005, *MNRAS*, 364, 407
- Chapman S. C., Smail I., Windhorst R., Muxlow T., Ivison R. J. 2004, *ApJ*, 611, 732
- Conselice C. J., Chapman S. C., Windhorst R. A. 2003, *ApJ*, 596, L5
- Di Matteo T., Springel V., Hernquist L. 2005, *Nature*, 433, 604
- Downes D., Solomon P.M. 1998, *ApJ*, 507, 615
- Fan X. et al. 2004, *AJ*, 128, 515
- Ferrarese L., Merritt D. 2000, *ApJ*, 539, L9
- Haas M., et al. 2003, *A&A*, 402, 87
- Haehnelt M., Kauffmann G. 2000, *MNRAS*, 318, L35
- Hao C. N., Xia X. Y., Mao S., Wu H., Deng Z. G. 2005, *ApJ*, 625, 78
- Heckman T. M., Kauffmann G., Brinchmann J., Charlot S., Tremonti C., White S. D. M. 2004, *ApJ*, 613, 109
- Isaak K. G., Chandler C. J., Carilli C. L. 2004, *MNRAS*, 348, 1035
- Isaak K. G., Priddey R. S., McMahon R. G., Omont A., Peroux C., Sharp R. G., Withington S. 2002, *MNRAS*, 239, 149
- Isobe T., Feigelson E. D., Nelson P. I. 1986, *ApJ*, 306, 490

- Kennicutt R. C. 1998, *ARA&A*, 36, 189
- Kim D.-C., Veilleux S., Sanders D. B. 1998, *ApJ*, 508, 627
- Kormendy J., Gebhardt K. 2001, in *AIP Conf. Proc.* 586, *Relativistic Astrophysics*, ed. H. Martel, J.C. Wheeler (New York: AIP), 363
- Kreysa E., et al. 1998, *Proc.SPIE*, 3357, 319
- Laor A. 1998, *ApJ*, 505, L83
- Magorrian J., et al. 1998, *AJ*, 115, 2285
- art05Martin D. C., et al. 2005, *ApJ*, 619, L59
- McMahon R. G., Priddey R. S., Omont A., Snellen I., Withington S. 1999, *MNRAS*, 309, L1
- Momjian E., Carilli C. L., Petric A. O. 2005, *AJ*, 129, 1809
- Omont A., Beelen A., Bertoldi F., Cox P., Carilli C. L., Priddey R. S., McMahon R. G., Isaak K. G. 2003, *A&A*, 398, 857
- Omont A., Cox P., Bertoldi F., McMahon R. G., Carilli C., Isaak K. G. 2001, *A&A*, 374, 371
- Omont A., McMahon R. G., Cox P., Kreysa E., Bergeron J., Pajot F., Storrie-Lombardi L. J. 1996, *A&A*, 315, 1
- Page M. J., Stevens J. A., Ivison R. J., Carrera F. J. 2004, *ApJ*, 611, L85
- Petric A. O., Carilli C. L. 2004, *IAUS*, 222, 535
- Priddey R. S., McMahon R. G. 2001, *MNRAS*, 324, L17
- Priddey R. S., Isaak K. G., McMahon R. G., Omont A. 2003, *MNRAS*, 339, 1183 (2003a)
- Priddey R. S., Isaak K. G., McMahon R. G., Robson E. I., Pearson C. P. 2003, *MNRAS*, 344, L74 (2003b)
- Robson I., Priddey R. S., Isaak K. G., McMahon R. G. 2004, *MNRAS*, 351, L29
- Rowan-Robinson M. 2000, *MNRAS*, 316, 885
- Sanders D. B., Soifer B. T., Elias J. H., Madore B. F., Matthews K., Neugebauer G., Scoville N. Z. 1988, *ApJ*, 325, 74 (1988a)
- Sanders D. B., Soifer B. T., Elias J. H., Neugebauer G., Matthews K. 1988, *ApJ*, 328, L35 (1988b)
- Shields G. A., Gebhardt K., Salviander S., Wills B. J., Xie B., Brotherton M. S., Yuan J., Dietrich M. 2003, *ApJ*, 583, 124
- Shields G. A., Menezes K. L., Massart C. A., Vanden Bout P. 2006, *ApJ*, 641, 683
- Silk J., Rees M. J. 1998, *A&A*, 331, L1
- Smail I., Chapman S. C., Blain A. W., Ivison R. J. 2004, *ApJ*, 616, 71
- Springel V., Di Matteo T., Hernquist L. 2005, *MNRAS*, 361, 776
- Staguhn J. G., Stern D., Benford D. J., Bertoldi F., Djorgovski S. G., Thompson D. 2005, *ApJ*, 629, 633
- Stern D., Spinrad H., Eisenhardt P., Bunker A. J., Dawson S., Stanford S. A., Elston R. 2000, *ApJ*, 533, L75
- Stevens J. A., Page M. J., Ivison R. J., Carrera F. J., Mittaz J. P. D., Smail I., McHardy I. M. 2005, *MNRAS*, 360, 610
- Tacconi L. J., et al. 2006, *ApJ*, 640, 228
- Tremaine S. et al. 2002, *ApJ*, 574, 740
- Treu T., Malkan M. A., Blandford R. D. 2004, *ApJ*, 615, L97
- Vestergaard M. 2004, *ApJ*, 601, 676
- Walter F. et al. 2003, *Nature*, 424, 406

Walter F., Carilli C., Bertoldi F., Menten K., Cox P., Lo K. Y., Fan X., Strauss M. A. 2004,  
ApJ, 615, L17

Zheng X. Z., Xia X. Y., Mao S., Wu H., Deng Z. G. 2002, AJ, 124, 18

**Table 1** Various Physical Parameters For 1.2 mm Detected QSOs

Name	Redshift	$S_{1.2\text{mm}}$	$\log(\frac{L_{\text{bol}}}{L_{\odot}})$	$\log(\frac{L_{60\mu\text{m}}}{L_{\odot}})$	$\log(\frac{\dot{M}_{\text{acc}}}{M_{\odot} \text{ yr}^{-1}})$	$\log(\frac{\dot{M}_{\star}}{M_{\odot} \text{ yr}^{-1}})$	$\log(\frac{\dot{M}_{\star}}{\dot{M}_{\text{acc}}})$
(1)	(2)	(3)	(4)	(5)	(6)	(7)	(8)
Carilli et al. (2001)							
J012403.78+004432.7	3.81	2.0±0.3	14.272	12.884	2.101	3.089	0.988
J015048.83+004126.2	3.67	2.2±0.4	14.094	12.939	1.923	3.283	1.360
J023231.40-000010.7	3.81	1.8±0.3	13.612	12.838	1.441	3.271	1.830
J025112.44-005208.2	3.78	2.4±0.6	13.691	12.966	1.520	3.411	1.891
J025518.58+004847.6	3.97	2.1±0.4	14.066	12.890	1.895	3.220	1.325
J032608.12-003340.2	4.16	1.5±0.4	13.885	12.726	1.714	3.045	1.331
J033829.31+002156.3	5.00	3.7±0.3	13.634	13.050	1.463	3.514	2.051
J111246.30+004957.5	3.92	2.7±0.5	13.997	13.004	1.826	3.402	1.576
J122600.68+005923.6	4.25	1.4±0.4	13.946	12.688	1.775	2.950	1.175
J123503.04-000331.8	4.69	1.6±0.4	13.523	12.709	1.352	3.129	1.777
J141205.78-010152.6	3.73	4.5±0.7	13.759	13.244	1.588	3.718	2.130
J141332.35-004909.7	4.14	2.5±0.5	13.840	12.950	1.669	3.367	1.698
J142647.82+002740.4	3.69	3.9±0.8	13.670	13.186	1.499	3.661	2.162
J144758.46-005055.4	3.80	5.4±0.8	13.644	13.316	1.473	3.803	2.330
J161926.87-011825.2	3.84	2.3±0.6	13.612	12.942	1.441	3.393	1.952
J235718.35+004350.4	4.34	1.8±0.6	13.639	12.789	1.468	3.206	1.738
Omont et al. (2001)							
PSSJ0209+0517	4.18	3.3±0.6	14.241	13.067	2.070	3.416	1.346
PSSJ0439-0207	4.40	2.3±0.7	14.003	12.891	1.832	3.246	1.414
PSSJ0808+5215	4.44	6.6±0.6	14.484	13.345	2.313	3.728	1.415
PSSJ1048+4407	4.40	4.6±0.4	13.963	13.192	1.792	3.639	1.847
PSSJ1057+4555	4.12	4.9±0.7	14.520	13.244	2.349	3.571	1.222
BRB1117-1329	3.96	4.1±0.7	14.278	13.181	2.107	3.564	1.457
BRB1144-0723	4.15	6.0±0.7	14.080	13.329	1.909	3.783	1.874
PSSJ1226+0950	4.34	2.8±0.7	13.963	12.981	1.792	3.380	1.588
PSSJ1248+3110	4.32	6.3±0.8	14.043	13.335	1.872	3.794	1.922
PSSJ1253-0228	4.00	5.5±0.8	13.878	13.305	1.707	3.775	2.068
PSSJ1317+3531	4.36	3.7±1.1	14.003	13.100	1.832	3.522	1.690
PSSJ1347+4956	4.56	5.7±0.7	14.325	13.271	2.154	3.671	1.517
PSSJ1403+4126	3.85	1.5±0.5	13.716	12.755	1.545	3.145	1.600
PSSJ1418+4449	4.32	6.3±0.7	14.443	13.335	2.272	3.726	1.454
PSSJ1535+2943	3.99	1.9±0.6	13.838	12.844	1.667	3.231	1.564
PSSJ1554+1835	3.99	6.7±1.1	13.638	13.392	1.467	3.883	2.416
PSSJ1555+2003	4.22	3.1±0.6	13.961	13.036	1.790	3.451	1.661
PSSJ1646+5514	4.04	4.6±1.5	14.479	13.224	2.308	3.557	1.249
PSSJ1745+6846	4.13	2.5±0.7	13.800	12.951	1.629	3.376	1.747
PSSJ1802+5616	4.16	2.8±0.9	13.761	12.997	1.590	3.438	1.848
PSSJ2322+1944	4.11	9.6±0.5	14.240	13.537	2.069	4.001	1.932
Omont et al. (2003)							
KUV08086+4037	1.78	4.3±0.8	13.739	13.443	1.568	3.933	2.365
093750.9+730206 <sup>a</sup>	2.52	3.8±0.9	14.368	13.304	2.197	3.704	1.507
HS1002+4400	2.08	4.2±0.8	14.273	13.400	2.102	3.840	1.738
HS1049+4033	2.15	3.2±0.7	14.235	13.273	2.064	3.693	1.629
110610.8+640008 <sup>a</sup>	2.19	3.9±1.1	14.677	13.355	2.506	3.674	1.168
140955.5+562827 <sup>a</sup>	2.56	10.7±0.6	14.329	13.749	2.158	4.227	2.069
154359.3+535903 <sup>a</sup>	2.37	3.8±1.1	14.283	13.322	2.112	3.744	1.632
HS1611+4719	2.35	4.6±0.7	14.043	13.408	1.872	3.875	2.003
164914.9+530316 <sup>b</sup>	2.26	4.6±0.8	14.240	13.418	2.069	3.866	1.797
high-z optically faint QSO							
030117+002025 <sup>c</sup>	5.5	0.87±0.20	12.374	12.387	0.216	2.878	2.662
High redshift QSOs with HCN/CO observations							
BRI1202-0725	4.693	12.59±2.28	14.407	13.657	2.236	4.120	1.884
BRI1335-0417	4.407	10.26±1.04	13.924	13.592	1.753	4.082	2.329
J1148+5251	6.419	5.0±0.6	14.388	13.095	2.217	3.396	1.179

Notes: Columns: (1) name. (2) redshift. (3) the observed flux density at 1.2 mm. (4) bolometric luminosity of AGN. (5) monochromatic luminosity at 60 $\mu\text{m}$  ( $\nu L_{\nu}$ ) (6) accretion rate of central supermassive black hole in  $M_{\odot} \text{ yr}^{-1}$ . (7) star formation rate in  $M_{\odot} \text{ yr}^{-1}$ . (8) the ratio of the star formation rate to the accretion rate. The objects from different samples are separated and labeled.

<sup>a</sup>The name with prefix [VV96]J.

<sup>b</sup>The name with prefix [VV2000]J.

<sup>c</sup>The name with prefix RDJ.

**Table 2** Binned data for 1.2mm non-detected QSOs

Number	mean redshift	weighted mean $S_{1.2\text{mm}}$	weighted mean $\log\left(\frac{L_{\text{bol}}}{L_{\odot}}\right)$	weighted mean $\log\left(\frac{L_{60\mu\text{m}}}{L_{\odot}}\right)$
Carilli et al. (2001)				
9	3.749	$0.190\pm 0.146$	13.915	$11.868\pm 0.333$
7	4.244	$0.092\pm 0.146$	13.860	$11.506\pm 0.689$
9	4.744	$0.187\pm 0.125$	13.821	$11.773\pm 0.290$
Omont et al. (2001) <sup>a</sup>				
44	4.232	$0.385\pm 0.128$	14.252	$12.129\pm 0.144$
Omont et al. (2003)				
19	2.172	$0.672\pm 0.210$	14.219	$12.593\pm 0.136$
7	2.529	$0.738\pm 0.287$	14.074	$12.592\pm 0.169$

Notes: The binned data for the 1.2mm non-detected QSOs in Carilli et al. (2001) and Omont et al. (2001, 2003). Columns: (1) the number of objects in each redshift bin with a bin width of 0.5. (2) the mean redshift in each bin. (3) the weighted mean flux density at 1.2 mm. (4) the average bolometric luminosity in each bin. (5) the weighted mean of the monochromatic luminosity at  $60\mu\text{m}$ .

<sup>a</sup>The redshift bin width is 0.56, which is the whole redshift range of this sample.

**Table 3** Various Physical Parameters for 850 $\mu\text{m}$  detected QSOs

Name	Redshift	$S_{850\mu\text{m}}$	$\log(\frac{L_{\text{bol}}}{L_{\odot}})$	$\log(\frac{L_{60\mu\text{m}}}{L_{\odot}})$	$\log(\frac{M_{\text{acc}}}{M_{\odot} \text{ yr}^{-1}})$	$\log(\frac{M_{\star}}{M_{\odot} \text{ yr}^{-1}})$	$\log(\frac{M_{\star}}{M_{\text{acc}}})$
(1)	(2)	(3)	(4)	(5)	(6)	(7)	(8)
X-ray Absorbed QSOs <sup>a</sup>							
005734.78–272827.4	2.19	11.7 $\pm$ 1.2	12.796	13.339	0.625	3.847	3.222
094144.51+385434.8	1.82	13.4 $\pm$ 1.5	12.774	13.426	0.603	3.935	3.332
094356.53+164244.1	1.92	3.0 $\pm$ 1.2	13.296	12.769	1.125	3.231	2.106
110431.75+355208.5	1.63	2.4 $\pm$ 1.2	12.917	12.691	0.746	3.174	2.428
110742.05+723236.0	2.10	10.4 $\pm$ 1.2	13.475	13.295	1.304	3.788	2.484
121803.82+470854.6	1.74	6.8 $\pm$ 1.2	12.625	13.137	0.454	3.644	3.190
124913.86–055906.2	2.21	7.2 $\pm$ 1.4	13.037	13.126	0.866	3.626	2.760
163308.57+570258.7	2.80	5.9 $\pm$ 1.1	13.181	12.992	1.010	3.481	2.471
Isaak et al. (2002)							
PSSJ0452+0355	4.38	10.6 $\pm$ 2.1	14.043	13.147	1.872	3.573	1.701
PSSJ0808+5215	4.44	17.4 $\pm$ 2.8	14.484	13.360	2.313	3.748	1.435
PSSJ1048+4407	4.40	12.0 $\pm$ 2.2	13.963	13.200	1.792	3.648	1.856
PSSJ1057+4555	4.12	19.2 $\pm$ 2.8	14.760	13.417	2.589	3.734	1.145
PSSJ1248+3110	4.32	12.7 $\pm$ 3.4	14.043	13.228	1.872	3.670	1.798
PSSJ1418+4449	4.32	10.4 $\pm$ 2.3	14.443	13.141	2.272	3.444	1.172
PSSJ1646+5514	4.04	9.5 $\pm$ 2.5	14.479	13.116	2.308	3.381	1.073
PSSJ2322+1944	4.11	22.5 $\pm$ 2.5	14.240	13.487	2.069	3.945	1.876
McMahon et al. (1999)							
BR2237–0607	4.55	5.0 $\pm$ 1.1	14.245	12.813	2.074	2.960	0.886
BRI0952–0115	4.43	14 $\pm$ 2	14.084	13.266	1.913	3.709	1.796
BR1033–0327	4.50	7 $\pm$ 2	14.045	12.962	1.874	3.332	1.458
BR1117–1329	3.96	13 $\pm$ 1	14.238	13.257	2.067	3.672	1.605
BR1144–0723	4.14	7 $\pm$ 2	14.000	12.978	1.829	3.367	1.538
BR1202–0725	4.69	42 $\pm$ 2	14.407	13.732	2.236	4.203	1.967
BRI1335–0417	4.40	14 $\pm$ 1	13.923	13.267	1.752	3.729	1.977
Priddey et al. (2003a) $z \sim 2$							
LBQSB0018–0220	2.56	17.2 $\pm$ 2.9	14.289	13.476	2.118	3.927	1.809
HSB0035+4405	2.71	9.4 $\pm$ 2.8	14.334	13.201	2.163	3.575	1.412
HSB0211+1858	2.47	7.1 $\pm$ 2.1	14.167	13.099	1.996	3.484	1.488
HSB0810+2554	1.50	7.6 $\pm$ 1.8	14.562	13.198	2.391	3.475	1.084
HSB0943+3155	2.79	9.6 $\pm$ 3.0	14.096	13.204	1.925	3.633	1.708
HSB1140+2711	2.63	8.6 $\pm$ 2.6	14.372	13.169	2.201	3.517	1.316
HSB1141+4201	2.12	8.6 $\pm$ 2.6	14.274	13.211	2.103	3.605	1.502
HSB1310+4308	2.60	10.0 $\pm$ 2.8	14.131	13.237	1.960	3.667	1.707
HSB1337+2123	2.70	6.8 $\pm$ 2.1	14.213	13.062	2.042	3.419	1.377
Priddey et al. (2003b) $z > 5$							
SDSSJ1306+0356	5.99	3.7 $\pm$ 1.0	13.977	12.646	1.806	2.847	1.041
SDSSJ1044–0125	5.74	6.1 $\pm$ 1.2	14.096	12.866	1.925	3.169	1.244
SDSSJ0756+4104	5.09	13.4 $\pm$ 2.1	13.650	13.223	1.479	3.703	2.224
SDSSJ0338+0021	5.07	11.9 $\pm$ 2.0	13.690	13.172	1.519	3.644	2.125

Notes: The columns have the same meanings as those in Table 1 but for detected QSOs at 850 $\mu\text{m}$ .

<sup>a</sup>The name with prefix RXJ.

**Table 4** Binned data for  $850\mu\text{m}$  non-detected QSOs

Number	mean redshift	weighted mean $S_{850\mu\text{m}}$	weighted mean $\log(\frac{L_{\text{bol}}}{L_{\odot}})$	weighted mean $\log(\frac{L_{60\mu\text{m}}}{L_{\odot}})$
X-ray absorbed QSOs <sup>a</sup>				
10	1.289	$0.772\pm 0.354$	12.652	$12.210\pm 0.199$
X-ray unabsorbed QSOs				
8	1.318	$0.405\pm 0.324$	12.854	$11.930\pm 0.347$
9	1.840	$0.717\pm 0.320$	12.935	$12.153\pm 0.194$
2	2.262	$0.379\pm 0.669$	12.993	$11.844\pm 0.766$
Isaak et al. (2002)				
30	4.214	$2.179\pm 0.533$	14.224	$12.468\pm 0.106$
McMahon et al. (1999)				
3	4.463	$3.167\pm 0.924$	14.203	$12.619\pm 0.127$
Priddey et al. (2003a) $z > \sim 2$				
10	1.765	$0.741\pm 0.829$	14.176	$12.173\pm 0.486$
27	2.190	$2.547\pm 0.546$	14.170	$12.677\pm 0.093$
11	2.725	$1.118\pm 0.871$	14.298	$12.275\pm 0.338$
Priddey et al. (2003b) $z > 5$				
6	5.100	$2.078\pm 0.726$	13.627	$12.413\pm 0.152$
3	5.577	$1.800\pm 0.884$	13.992	$12.339\pm 0.213$
1	6.280	$1.300\pm 1.000$	13.979	$12.189\pm 0.334$

Notes: The binned data values for non-detected QSOs (at levels of  $3\sigma$ ) at  $850\mu\text{m}$ . The columns have the same meanings as those in Table 2 except that col(3) is the weighted mean flux density at  $850\mu\text{m}$ . Note that some redshift bin widths are slightly different from 0.5 as the sample redshift range is slightly larger or smaller than 0.5. <sup>a</sup>One QSO at  $z=2.46$  with a flux density of  $-1.6 \pm 1.2$  at  $850\mu\text{m}$  was not included in the estimation because of its large redshift compared to the other non-detected QSOs (with  $z \leq 1.5$ ).



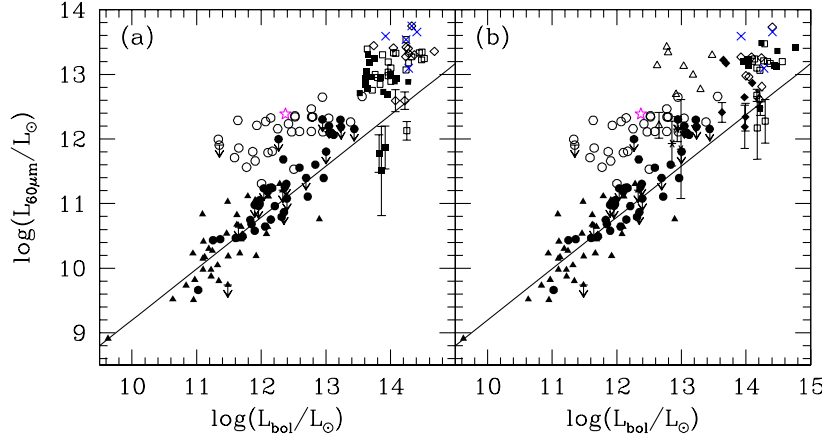


**Fig. 1** The monochromatic luminosity at  $60\mu\text{m}$  vs. the bolometric luminosity of AGN for low- $z$  objects and high- $z$  QSOs observed (a) in the mm and (b) in the submm. In both panel (a) and (b): the open circles represent IR QSOs; the filled circles and triangles represent PG QSOs and NLS1s respectively; the crosses are for the three QSOs with CO and/or HCN observations; the pentagram represents the distant ( $z = 5.5$ ) optically faint ( $M_B \sim -24.2$ ) QSO (see text); the solid line is the best regression line for the local PG QSOs and NLS1s obtained from survival analysis; the data points with error bars indicate they are the binned values for (sub)mm non-detected QSOs (see Sect. 4.1). In panel (a), the open and filled squares represent the QSOs taken from Omont et al. (2001) and Carilli et al. (2001) respectively; the diamonds represent the QSOs from Omont et al. (2003). In panel (b), the open triangles indicate the X-ray absorbed QSOs taken from Stevens et al. (2005); the open and filled squares represent objects from Priddey et al. (2003a) and Isaak et al. (2002) respectively; the open and filled diamonds indicate the QSOs obtained from McMahon et al. (1999) and Priddey et al. (2003b). The stars with error bars are the binned data for X-ray unabsorbed, submm non-detected QSOs from Page et al. (2004).

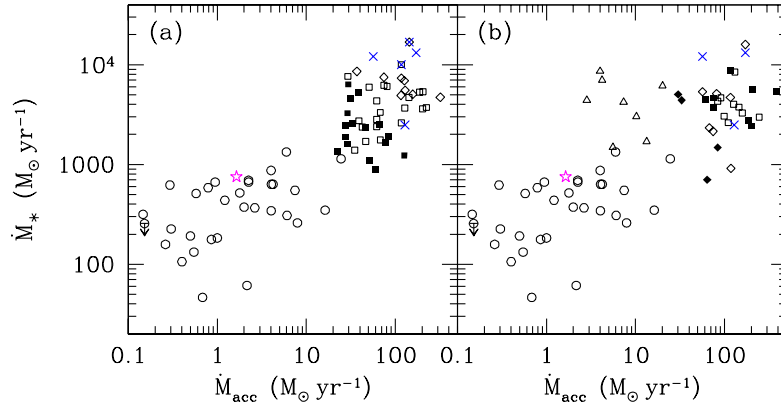


**Fig. 2** The star formation rate ( $\dot{M}_*$ ) vs. the accretion rate ( $\dot{M}_{\text{acc}}$ ) for local IR QSOs and high- $z$  QSOs detected (a) in the mm and (b) in the sub-mm. The symbols are the same as in Fig. 1.

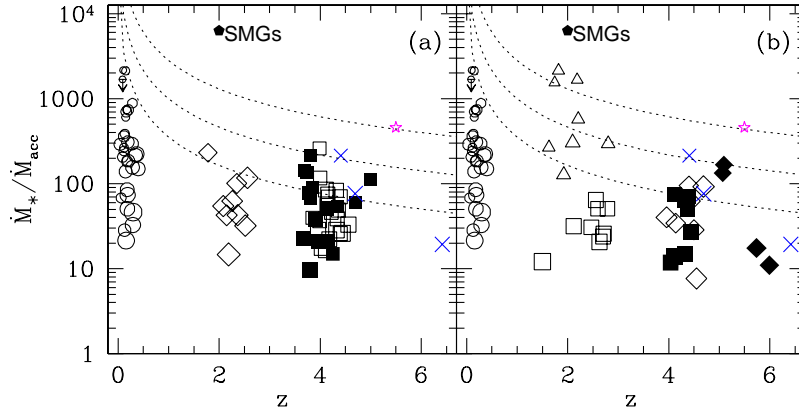


**Fig. 3** The ratio of  $\dot{M}_*$  and  $\dot{M}_{acc}$  vs. redshift for local IR QSOs and (a) high-z mm detected QSOs and (b) high-z submm detected QSOs. The symbols are the same as in Fig. 1. The sizes of the data points indicate their bolometric luminosities associated with AGNs. The dotted lines are for three flux limits which correspond to a bolometric luminosity of  $10^{11}L_\odot$ ,  $10^{12}L_\odot$  and  $10^{13}L_\odot$  (from top to bottom) at redshift 2 respectively. For each curve, we assume the relation between the star formation rate and the accretion rate by simply fitting a regression line to the data points in Fig. 2a using survival analysis.